# Linking CO_2 Sorption Performance to Polymer Morphology in Aminopolymer/Silica Composites through Neutron Scattering

Adam Holewinski, Miles A. Sakwa-Novak, and Christopher W. Jones*

School of Chemical & Biomolecular Engineering, Georgia Institute of Technology, 311 Ferst Drive, Atlanta, Georgia 30332, United States

S *Supporting Information*

ABSTRACT: Composites of poly(ethylenimine) (PEI) and mesoporous silica are effective, reversible adsorbents for CO_2, both from flue gas and in direct air-capture applications. The morphology of the PEI within the silica can strongly impact the overall carbon capture efficiency and rate of saturation. Here, we directly probe the spatial distribution of the supported polymer through small-angle neutron scattering (SANS). Combined with textural characterization from physisorption analysis, the data indicate that PEI first forms a thin conformal coating on the pore walls, but all additional polymer aggregates into plug(s) that grow along the pore axis. This model is consistent with observed trends in amine-efficiency (CO_2/N binding ratio) and pore size distributions, and points to a trade-off between achieving high chemical accessibility of the amine binding sites, which are inaccessible when they strongly interact with the silica, and high accessibility for mass transport, which can be hampered by diffusion through PEI plugs. We illustrate this design principle by demonstrating higher CO_2 capacity and uptake rate for PEI supported in a hydrophobically modified silica, which exhibits repulsive interactions with the PEI, freeing up binding sites.
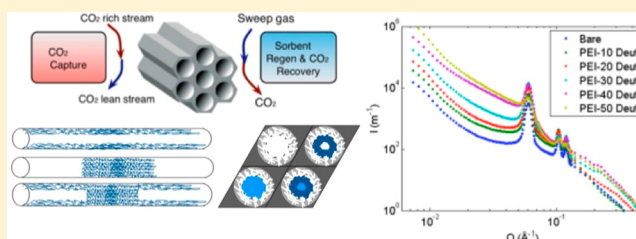
INTRODUCTION

Supported amines are a valuable class of materials for numerous catalysis[1−3] and separation applications.[4−11] Most notably, they are effective in reversible CO_2 adsorption.[12−15] As scientific consensus on the link between anthropogenic CO_2 and climate change continues to solidify, these materials are increasingly being incorporated into scalable carbon capture processes.[16,17] Mesoporous silica materials are versatile supports for amine moieties and can be synthesized with optimal pore sizes to balance gas transport and amine dispersion. A particularly useful model silica system is SBA-15, as it possesses well-ordered and monodisperse pores, arranged as a hexagonal lattice of parallel cylinders (depicted in Figure 1).[18,19] In studies using well-defined mesoporous oxide supports, the role of support pore size, composition and particle size on the adsorption capacity and efficiency have been studied in detail.[20−30]

Amino-polymers, most often poly(ethylenimine) (PEI), are the most studied and arguably the most effective amine-containing additives in these systems, as they have low volatility and possess a high density of amine sites for CO_2 adsorption. As would intuitively be expected, the CO_2 capacity (mmol CO_2/g sorbent) of amino-polymer/silica composites generally increases with polymer loading. This relationship is shown in Figure 1 for a typical series of PEI/SBA-15 composites adsorbing CO_2 from simulated dry air. The figure also shows the capacity is not directly proportional to the amine loading, and the important metric of amine efficiency (mol CO_2/mol N) tends to rise when moving from low to intermediate amine

loadings. Thus, the utilization of amine sites increases as the pores are filled to higher fractions.[12,20,21,31]

A maximum in the amine efficiency is set by the reaction chemistry between amines and CO_2, where the primary product is believed to be alkylammonium carbamate ion pairs, formed through a zwitterionic mechanism. This chemistry is well established in liquid solutions,[32] and it has been extrapolated to solid systems with spectroscopic support.[33−36] Under anhydrous conditions, two amines are required in the immobilization of one CO_2, setting the amine efficiency limit at one-half. Sorbents also usually exhibit a plateau in capacity with respect to PEI loading because the diffusivity of CO_2 through the polymer slows dramatically during the course of saturation,[37,38] likely due to CO_2-induced cross-linking.[39,40] Ultimately, it is expected that the adsorption capacity and kinetics will depend heavily on the morphology of the polymer, i.e., whether it prefers to coat the pore walls or form agglomerates, and/or the extent to which each occurs. Thus, an informed performance optimization requires a detailed understanding of the interrelation between polymer and support morphologies. Despite this critical need, there are no published reports that differentiate and directly probe the morphology of the impregnated polymer phase in amine/oxide composite CO_2 adsorbents.

In the present contribution, we use small angle neutron scattering (SANS) to probe the morphology of PEI in the pore
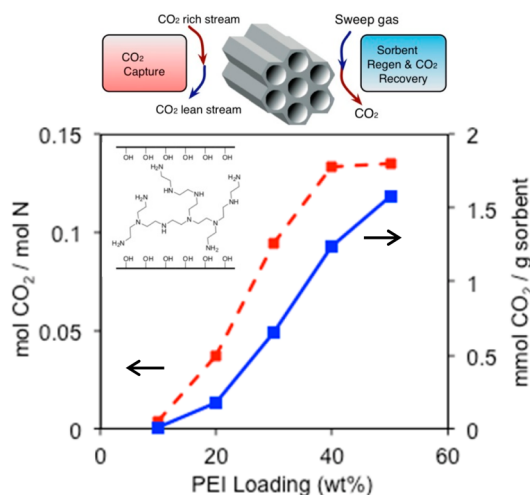
Figure 1. Top: Schematic process for CO_2 adsorption and recovery. The hexagonally packed cylinder structure is exhibited by SBA-15 silica supports. Bottom: CO_2 capacity for a typical PEI/SBA-15 composite as a function of PEI ($M_w \sim 800$ Da) loading, in 400 ppm of CO_2/He at 25 °C, with corresponding amine efficiencies. Inset: low molecular-weight poly(ethylenimine) in a silica pore.

space of two SBA-15 type silicas as a function of PEI loading. We examine the scattering profiles in the context of other morphological characterizations, including N_2 physisorption isotherms and electron microscopy images, as well as simulated scattering models. Our analysis suggests that PEI initially forms a thin coating, adhering to the surface of the pore walls at low loadings, while increasing the PEI loading results in plug-like agglomerates forming after the initial coating. We also find that the plugs of PEI are narrower (on the order of 1 nm) than the pore diameters derived from physisorption, in accord with the proposition of a pore-perimeter-region containing silica of reduced density, often referred to as a corona.[41,42] The evidence suggests that the corona region contains a boundary with significant open volume that can mimic a wider pore when probed by N_2, but that PEI does not necessarily permeate this space; i.e., the corona can be dominated by either surface corrugation[43] or narrow micropores,[44−47] depending on synthetic conditions.

Finally, we compare the CO_2 adsorption performance of these materials against the polymer morphology model. We infer that at low polymer loadings, oxide surface-binding restricts the chemical accessibility of the amines for CO_2 adsorption, leading to low amine efficiencies. Conversely, higher loadings exhibit increased CO_2 diffusional barriers due to formation of plugs of PEI within the pores. These chemical and diffusional accessibility factors must be balanced for optimal adsorbent performance. As a demonstration of this design principle, we synthesize an SBA-15 variant with a trimethylsilyl-functionalized surface, for which we hypothesize PEI to exhibit weaker silica surface adsorption. Adsorbents prepared from this support material demonstrate faster CO_2 uptake rates and higher total capacities than their surface silanol-containing counterparts.

■ EXPERIMENTAL SECTION

Silica Synthesis. SBA-15 was prepared by adapted protocols from our prior work[2,22] (SBA15−100), and from the literature[46,48] (SBA15−130). In each case, block copolymer Pluronic 123 ($EO_{20}PO_{70}EO_{20}$, Sigma-Aldrich) was dissolved and allowed to

equilibrate under acidic conditions (forming an organic template for silica condensation), prior to addition of tetraethylorthosilicate (TEOS, Sigma-Aldrich) and subsequent silica condensation, hydrothermal treatment, and calcination steps. For SBA15−100 preparation, 24 g of P123 were first dissolved in a 2L Erlenmeyer with 636 g of DI water and 120 mL of fuming HCl (BDH) and stirred for 3 h. Next, 52.6 g of TEOS was added dropwise, and the solution stirred another 24 h at 40 °C. Stirring was then stopped and the material was held at 100 °C for 24 h. The SBA15−130 was prepared in a sealed 700 mL Berghof synthesis reactor equipped with an impeller. Here, 12 g of P123 was dissolved in 61.7 g of fuming HCl and 388.3 g of H_2O. The solution was stirred at 600 rpm for 3 h at 40 °C. Then, 25.5 g of TEOS was poured into the container and the mixture stirred at 600 rpm for 5 min, then stopped. The material was then statically aged at 40 °C for 24 h before hydrothermal treatment at 130 °C for 48 h. After the hydrothermal treatments, all SBA-15 samples were filtered and rinsed with water, then dried overnight at 75 °C. All samples were then calcined at 550 °C for 6 h.

The surface of a portion of the SBA-15 was modified with trimethylsilyl groups via the grafting of hexamethyledisilazane (HMDS, Sigma-Aldrich). Here, 2 g of dried SBA-15 was dispersed in 100 mL of anhydrous toluene in a sealed flask and allowed to equilibrate for 1 h. Then, 1.2 g of HMDS was added via syringe and the solution was stirred at 80 °C for 24 h before filtering, washing with toluene, and vacuum drying at ∼80 °C.

Poly(ethylenimine) Synthesis. Synthesis of poly(ethylenimine)-d_5 (d-PEI) is described in detail along with characterization in the Supporting Information. Briefly, d-PEI was synthesized by the acid-catalyzed polymerization of ethylenimine-d_4 in the presence of ethylenediamine-d_4 (CDN Isotopes) as a capping agent. The ethylenimine monomer was prepared by bromination of ethanol-amine-d_4 (CDN Isotopes) to bromoethylamine-d_4 by heating in HBr, followed by base-activated ring closure and concentration by distillation. Final sample impregnation on the SBA-15 support was done in MeOD (CDN) to achieve H/D exchange for the labile hydrogen. Hydrogenated PEI (h-PEI) was purchased ($M_w \sim 800$, Sigma-Aldrich).

Silica/PEI Composite Preparation. PEI/SBA-15 composites were prepared by mixing, equilibrating and drying solutions of PEI and SBA-15 in MeOD (CDN) with a rotatory evaporator. For each sample, 30 mL MeOD, 250 mg SiO_2 and a chosen amount of PEI were used. PEI and SiO_2 were added to methanol separately, stirred for 1 h and then combined and further stirred for 3 h before solvent removal. Final degassing was performed in a Schlenk flask on a high vacuum line (∼10 mTorr) under a vacuum at 110 °C to remove any CO_2 and residual solvent. Samples were transported under a vacuum into a helium glovebox for further handling.

Chemical Structure Characterization. Poly(ethylenimine)-d_5 and synthetic intermediates were probed by ^2H NMR and ^{13}C NMR on a Bruker DRX 500 spectrometer. All samples were prepared in distilled H_2O solvent. For the ^{13}C measurements, all T_1 relaxation times were first determined, and scan times were allotted to yield quantitative spectra. No decoupling sequences were needed as C/D coupling only yielded slightly broadened peaks. Spectra demonstrating product purity and distribution of primary, secondary, and tertiary amines (defining branching rate) from the ^{13}C spectra are shown in the Supporting Information. The molecular weight was estimated by gel-permeation chromatography using a Shimadzu HPLC system with refractive index detector (RID-10A) and Viscotek TSK Viscogel PWXL Guard, G3000, G4000, and G6000 columns (in series). Samples were prepared at ∼30 mg/mL in an eluent phase of 0.1 M sodium nitrate +0.1 M acetic acid and flowed at 1 mL/min. The synthetic PEI elution time was compared to commercial samples of branched PEI at M_W 800, 1200, 1800, 2000, and 25 000. Elution of the synthetic PEI came between the 800 and 1200 Da reference samples.

Physisorption and Analysis. All nitrogen physisorption isotherms were collected on a Micromeritics Tristar 3020 instrument at 77K. Samples were degassed at 110 °C for 12 h prior to measurement. Pore volume and pore size distributions were calculated from the adsorption isotherms using the NLDFT equilibrium model[49,50] in the

Quantachrome VersaWin software package. Surface areas were determined by the BET method.

CO₂ Adsorption and Amine Loading. Dry CO_2 capacities were measured using a TA Instruments Q500 TGA. Samples were exposed to 400 ppm of CO_2/He at 30 °C for 12 h and the corresponding weight gain was recorded and normalized by the dry weight of sample used. Samples were pretreated under He flow at 110 °C for 3 h prior to exposure to CO_2 containing gas. Amine content of the samples was measured using a Netzch STA409PG TGA. Weight loss from 120 to 900 °C under a flow of nitrogen diluted air was recorded and normalized by the residual mass at 900 °C.

Imaging. Transmission electron microscopy was performed on an FEI Tecnai F30 field emission gun microscope at 300 keV accelerating voltage. Samples were prepared by sonicating 5 mg/mL silica powder in methanol and pipetting a drop onto a Cu grid with Formvar coating. Scanning electron microscopy was performed on a Hitachi SU8010 at 5 keV. Samples were prepared on a carbon tape substrate.

Scattering Experiments. All small-angle neutron scattering samples were dry powders in gastight aluminum holders with 1 mm path length and 1 in. diameter quartz windows. Sample weights were chosen to maintain a constant 100 mg silica basis (e.g., a 50% wt. PEI sample would be 200 mg total sample mass). All assembly was performed under helium in a glovebox. SANS was performed on the EQ-SANS instrument[51] at the Spallation Neutron Source at Oak Ridge National Lab. Two instrument configurations were used to access a wide q-range and establish an incoherent background intensity for subtraction. Low q data were acquired with a detector distance of 5 m and neutron wavelength of 6 Å. High q data were acquired with a 1.3 m detector distance and 1 Å neutron wavelength. These configurations had a q-uncertainty of less than 5% for all $q > 0.01$ Å^{-1}.[51] The two spectra for each sample were stitched with an overlap region from 0.13 to 0.14 Å^{-1} and calibrated to absolute intensity using a silica standard (Porasil). No adjustments for SBA-15 packing fraction were made.

■ RESULTS

Morphology Analysis of PEI/SBA-15 by Physisorption. Nitrogen physisorption isotherms were used to assess textural characteristics of the PEI/silica composites including surface area, pore volume, and pore-size-distribution. PEI weight-loadings ranging from 0 to 50% (nominal) were investigated (exact loadings in Table S1). Two separate material loading-series were prepared using two batches of SBA-15, chosen to assess the impact of textural differences such as particle size, pore dimensions, and degree of intrawall porosity or surface roughness. These supports were synthesized as described elsewhere,[18,46,48] with the main differentiating factor being hydrothermal treatment at 100 °C for 24 h (denoted SBA15−100) and 130 °C for 48 h (denoted SBA15−130). In the case of SBA15−130, synthesis conditions were selected to optimize the mesostructure with minimal nonidealities (intrawall pores etc.).[46,48] In contrast, the SBA15−100 was prepared as a standard to match many previous reports by our group and others on PEI/SBA-15 adsorbents. In Figure 2, we show SEM images of the silica particles comprising each material, as well as TEM images depicting their internal mesopore structure. It can be seen that the SBA15−130 generally exhibits larger, more uniform particles with wider pores compared to the standard SBA15−100.

N₂ physisorption isotherms for each of the bare SBA-15 support materials are presented in Figure 3a. The pressure regime of largest volume uptake (region (iii)) corresponds to capillary condensation in the primary mesopores of the material, while the sharp condensation feature at low pressure (region (i)) is generally attributed to narrow, intrawall micropores,[52] illustrated schematically in the inset of the figure.
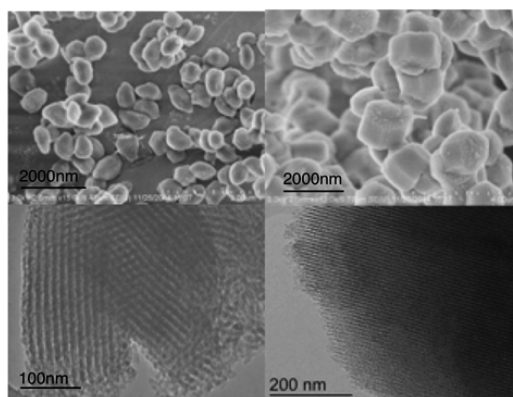

Figure 2. Representative SEM (above) and TEM (below) images for SBA15−100 (left) and SBA15−130 (right).

Region ii (intermediate pressure) of the isotherms corresponds mainly to multilayer adsorption of N₂; a higher slope in this region should correspond to increased surface roughness (more area) along the mesopores, as implied by the BET equation.[53] The isotherms together indicate that the SBA15−130 contains higher specific pore volume and decreased microporosity compared to SBA15−100, making it a more ideal cylindrical array and a presumptively better model system for scattering studies.

Upon introduction of PEI, a very rapid drop in surface area (BET method) is seen at small loadings, as shown in Figure 3b. Likewise, pore volumes (NLDFT method)[49,50,54] show an initial decrease that is disproportionately large relative to the volume of added PEI itself. This suggests that smaller intrawall pores or surface corrugations may become blocked off, rather than filled. This blocked intrawall porosity is less prevalent on the SBA15−130 material, likely because it has larger and less numerous intrawall pores.[44,46,47] It is noteworthy that the surface areas converge to similar values once the smallest micropores are blocked. Corresponding isotherms (used to determine the surface area and pore volume) for the full PEI-loading series on both support materials are contained in Figure S1.

We note that all physisorption data presented are from samples used for scattering characterization, which required fully deuterated PEI (d-PEI, synthesized in-house). Composite sorbents prepared from this surrogate polymer showed CO_2 adsorption capacity that was comparable, but ~20% lower than analogues prepared from commercial PEI, as shown in Figure S2. The d-PEI had similar molecular weight to commercial PEI's used in composite sorbents ($M_w \sim 1000$), while the ratio of 1°:2°:3° amines was 20:48:32, compared to 44:33:23 in commercial PEI[55] (quantitative ¹³C NMR and ²H NMR in Figures S7−S8). Primary amines are the most effective at CO_2 capture, largely accounting for the capacity difference.

Further morphological information can be extracted from pore-size distribution (PSD) analyses, shown in Figure 4. Using the NLDFT equilibrium PSD method, the bare SBA15−100 shows distinct volume contributions from pores with diameters below 3 nm. These pores disappear at 10% wt PEI loading, which corresponds to roughly a monolayer relative to the mesopore surface area. Additional increases in PEI loading appear to cause a contraction of the apparent diameter from ~8.2 nm to ~7 nm, after which the pore volume decreases with no change in diameter. Although the calculated size distribution is predicated on numerous assumptions—mainly that N₂
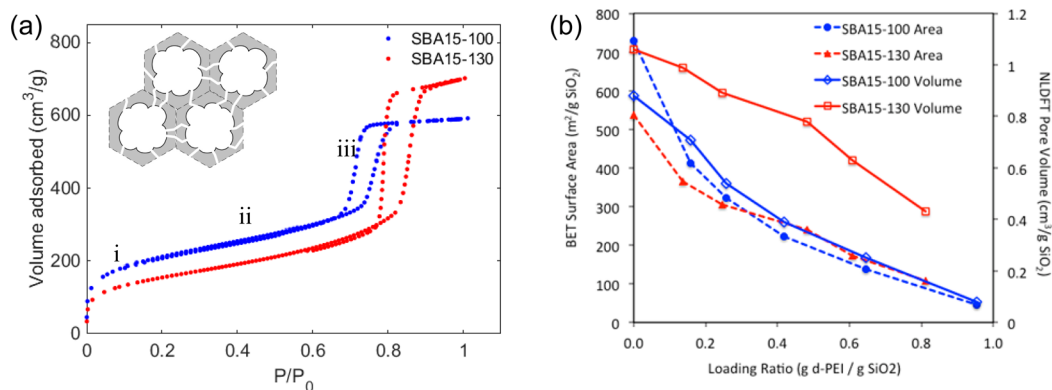
Figure 3. (a) N_2 physisorption isotherms for the each SBA-15 support at 77K, showing differences in microporosity and pore volume. Inset: Schematic two-dimensional cross-section of SBA-15 (b) Summary of BET surface area and NLDFT pore volume vs PEI-loading on each material.
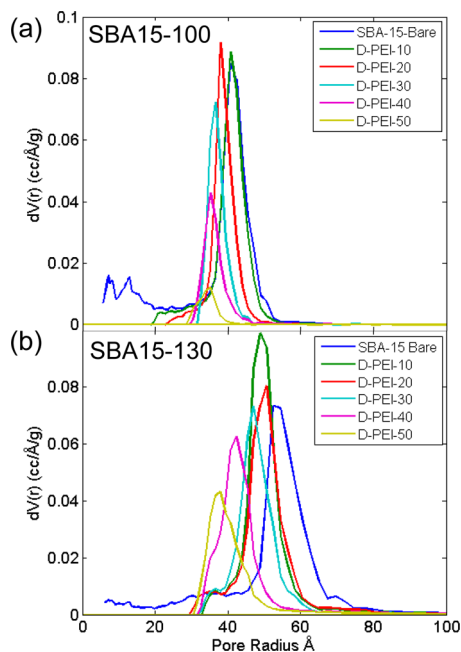

Figure 4. Pore size distributions calculated from N_2 physisorption isotherms using the NLDFT method and a cylindrical silica pore model for samples of SBA15−100 (a) and SBA15−130 (b) with d-PEI loadings ranging from 0 to 50% wt. Introduction of the polymer causes an initial drop in apparent radius, which levels off at higher loading.

adsorption is occurring in perfect cylinders of SiO_2 with no polymer coating—one could tentatively interpret the PSD to indicate that PEI deposition begins as a conformal coating of the mesopore (having an annular shape). After reaching some critical thickness, PEI may then begin to aggregate (likely due to less attraction to the polymer coated wall than the bare, silanol-laden wall) taking the approximate shape of a cylindrical plug that grows in the axial direction of the pore with further amine loading. Such a deposition mechanism would permit a decrease in volume with no change in diameter distribution after a critical polymer loading. While the aforementioned physisorption trends have been reported in numerous instances throughout the adsorption literature,[20,55,56] the present interpretation of sequential coating and plug formation (supported further below with scattering data) is the first clear explanation of the observed threshold diameter phenomenon.

In the case of SBA15−130, the shift in pore diameter at low PEI loadings is even more pronounced than on SBA15−100. We suspect that surface corrugation or larger intrawall porosity (the distinction is not necessarily apparent) is more dominant than narrow micropores in this material, as evidenced additionally by larger N_2 volumes adsorbing in the multilayer pressure regime of the isotherms. Such corrugation could be manifested as a larger apparent pore radius in the PSD rather than distinct smaller pores. As PEI begins to coat (and possibly fill) the corrugations, the apparent diameter drops significantly from ∼10.8 to ∼8 nm. It is also worth noting that due to the higher pore volume of SBA15−130, 50% wt nominal loading of PEI only achieves a fill fraction of ∼60% of the total measurable void space in this material. Higher PEI loading tests confirm a similar trend in PSD evolution to the SBA15−100 materials, and the apparent pore diameter does not fall below 7 nm.

Scattering Properties of PEI/SBA-15 Systems. Small angle neutron scattering is well suited to probe the geometric properties of each phase in PEI/SBA-15 composites due to differences in the neutron scattering-length density (SLD) of the polymer and that of the silica matrix. However, achieving a strong contrast requires replacement of the hydrogen atoms on PEI with deuterium, which scatters neutrons more strongly and coherently (reducing noise). Thus, composites for this study were prepared with fully deuterated PEI (d-PEI), synthetically tailored to possess similar properties to commercial PEI (characterization in SI).

In Figure 5 we show the scattering intensity of the bare SBA-15 supports as a function of the magnitude of neutron momentum transfer, $q = (4\pi \sin(\theta)/\lambda)$, where θ is the scattering angle and λ is the wavelength. Intensities are given in absolute units of differential cross-section per volume (m^{-1}) and were calibrated from a standard sample. To a reasonable approximation, structural motifs of vastly different length scales can be considered to dominate scattering within their own characteristic q-regimes, where $q \sim (2\pi/d)$, and d is the distance in real space. For both silica samples, the particle size corresponds to q-values well below the range of measurement, but scattering from the external surface of the particles still contributes intensity at the lowest measured q-values and is proportional to q^{-4} (Porod's law, illustrated in Figure 5). At intermediate q-values, the particle surface contribution decays below that of the internal structure, which should in principle be controlled by scattering of mesoscale features. However, it is commonly observed in amorphous silica systems that a relatively high concentration of smaller scale (and very
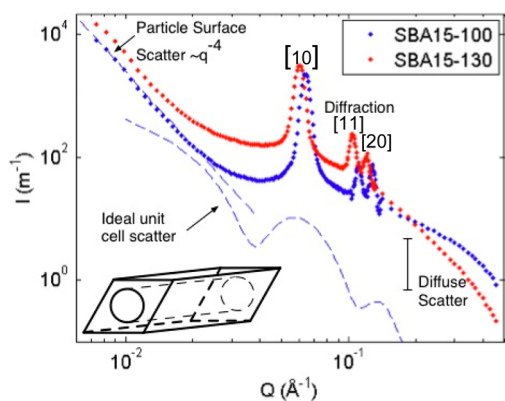
Figure 5. SANS patterns of SBA15−100 (blue) and SBA15−130 (red), along with calculated scattering characteristics of an ideal mesoporous particle with smooth boundaries at low and intermediate q (dashed curves). The SBA15−130 contains larger and fewer intrawall pores or corrugations than SBA15−100, and consequently shows less diffuse scattering at high q.

polydisperse) inhomogeneities creates a broad, smooth scattering characteristic that masks the mesopore scattering, with the exception of diffraction peaks (the collective interference pattern of the mesopores), which rise above the baseline intensity.[57−61] We demonstrate this in Figure 5 with an overlay of the calculated scattering pattern of a smooth 80 Å pore inside a solid 120 Å hexagonal lattice primitive cell (details in Supporting Information). A rapid decay into a second Porod (q^{-4}) regime, corresponding to internal surface scatter, would be expected at much lower q-values than seen in experiment due to smaller features such as micropores.

To adopt a more quantitative framework for discussion, we consider that a simple scattering pattern may be described by the product of a form factor, $P(q)$, related to the shape of a scattering body, and a structure factor, $S(q)$, related to the

relative locations of the scattering bodies. These quantities are given respectively by the squared magnitude of the Fourier transform (FT) of the SLD distribution defining the shape, and the FT of a lattice describing the locations of the centers of mass across the ensemble of shapes. The present scattering system may be represented as an array of unit cells that (i) form a hexagonal lattice, and (ii) are hierarchically arranged in the form of a particle. In this general description, we may posit a scattering law (derived in the Supporting Information) given by

$$I(q) = \frac{N_p}{V}\{N_C P_C(q)\cdot[S(q) + N_C P_{P0}(q)] + i_D(q)\} \qquad (1)$$

where $P_C(q)$ is the form factor of the unit cell, N_C is the number of cells in a particle, $S(q)$ is the structure factor for the hexagonal lattice, P_{P0} is the normalized form factor (per squared unit volume and SLD) of the macroscopic particle (rapidly decaying at low-q), and $i_D(q)$ is a function describing the diffuse background scattering of small scale inhomogeneities (to be defined later). The set of terms in square brackets may be thought of as a total structure factor and is applicable for $V_{particle} \gg V_{cell}$. We note that $S(q) \approx 1 + \Sigma_{hk}\delta(q_{hk})$, where the delta functions peak at reciprocal lattice plane separations. The term of unity means the baseline intensity at intermediate q contains a sum of the unit cell form factor $P_C(q)$ and the diffuse scattering function $i_D(q)$, while the diffraction peak intensities are modulated by the magnitude of $P_C(q)$ alone. The form factor and diffuse function both technically represent "diffuse" scattering, but for clarity we refer to only the latter as such.

The weak scattering by the bare mesostructure relative to the smaller scale imhomogeneities in SBA-15 and other hexagonal silicas has often relegated determination of structural parameters (e.g., pore size or density gradients) with SANS or SAXS to comparison of relative diffraction peak heights.[42,45,62−72] However, full-pattern fitting has been of use in modeling characteristics of adsorbed films or pore-filling
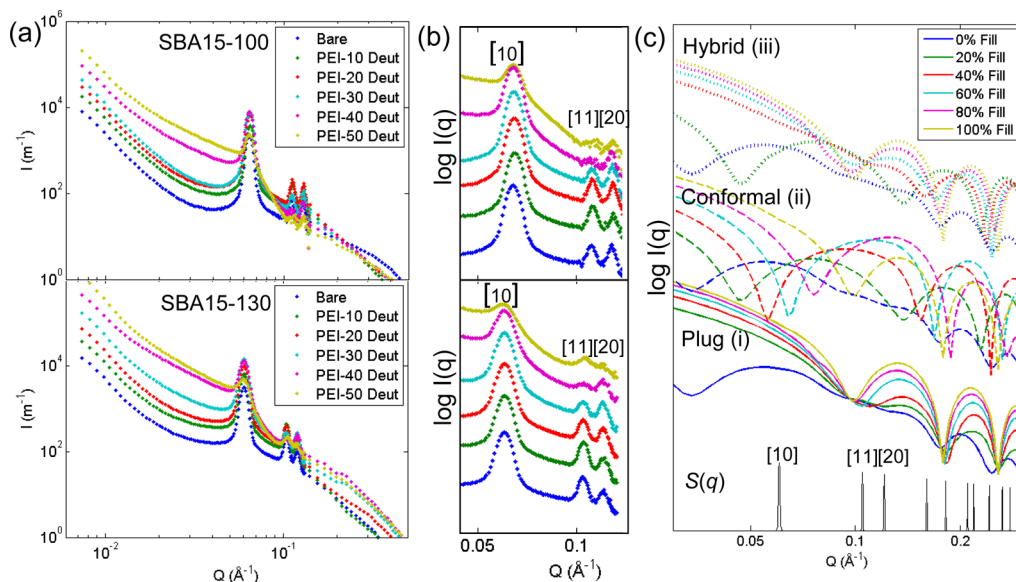

Figure 6. (a) SANS patterns collected for both d-PEI/SBA-15 systems ranging from 0 to 50 wt % nominal loading of polymer (0−90% fill fraction for SBA15−100 and 0−60% fill fraction for SBA15−130). (b) Bragg regions of the same patterns, shifted for visibility (c) Calculated form factors for SBA-15 unit cell with varying fill fraction for each general motif depicted in Figure 7 and discussed in the text. An ideal hexagonal lattice structure factor is overlaid for reference. Parameters used in the calculation were a = 120 Å, R_p = 40 Å, R_c = 50 Å, and L = 10 000 Å. Relative intensities are self-consistent within each cluster of curves, but each cluster is shifted vertically for visibility.

agents, particularly with SANS.[58,60,73−78] Addition of a high-contrast pore occupant such as d-PEI intensifies the mesostructure scattering. On the basis of component atomic scattering-lengths,[79] we estimate the SLD of d-PEI to be $\sim 8.2 \times 10^{-6}\ \text{Å}^{-2}$, compared to ∼$3.5 \times 10^{-6}\ \text{Å}^{-2}$ for amorphous SiO_2 (nonporous), yielding a scattering cross-section ratio (squared ratio of SLDs) of at least five—larger in practice due to small or occluded porosity in the silica phase.

In Figure 6a, we show SANS patterns for the full 0−50% wt d-PEI-loading series on SBA15−100 and SBA15−130. Spectra were taken with an equal silica-mass basis so that the differences in intensity directly reflect changes to the volumetric fill fraction of the PEI polymer. The incremental addition of PEI raises the total scattered intensity and generates several unique changes to the shape of the scattering pattern. To the left of the [10] Bragg peak, the intensity takes on an increasingly pronounced linear characteristic (intensity $\propto q^{-1}$), suggestive of high aspect-ratio prism structures such as a cylinder or elongated shell.[80] The [10] peak concomitantly takes on an increasingly asymmetric shape. These features are both direct manifestations of the mesoscale unit cell scattering, which was not directly observable from the empty SBA-15. It can also be seen that the [11] and [20] Bragg peaks undergo a relative inversion in intensity. Collectively, these changes provide a signature of the PEI deposition morphology, which we make use of and discuss below in the context of modeling and data fitting.

SANS Model for PEI Deposition. A variety of morphological filling motifs for PEI within the SBA-15 pores can be envisioned based on the interaction of the polymer with the pore wall. A strongly attractive interaction would be expected to yield an adsorbed coating, and this interaction could potentially extend to many conformal layers. Conversely, inert or repulsive walls should lead to preferential aggregation of the polymer as it minimizes interfacial area.

To assess the possible modes of polymer filling, including various intermediate cases, we explicitly modeled the PEI as (i) a conformal polymer coating (an annular shell of growing thickness at the pore wall, surrounding an open core), (ii) a single polymer plug (same diameter as pore, growing lengthwise with filling), and (iii) various hybrid structures where polymer filling creates both a plug and a conformal coating. The hybrid case was examined both sequentially (shifting to a plug after reaching a critical shell thickness) and simultaneously (both structures growing in different proportions at the same time). Schematics of each general filling motif are shown in Figure 7. We also considered the possibility of a reduced-density corona region spanning an annular space of unknown thickness at the pore perimeter. Though this region
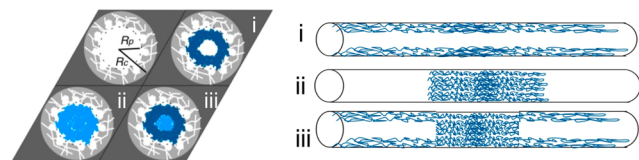

Figure 7. Schematic of the proposed SBA-15 morphology and various PEI-filling motifs. The pore is modeled as containing an empty cylindrical region of radius R_p and an annular region of reduced density (relative to the bulk SiO_2), with outer radius R_c. PEI may fill the pore conformally (i), as an aggregate (ii), or as a mixture of these modes (iii), either sequentially (coating up to critical thickness, then forming a plug) or simultaneously (both regions coexisting at all fill fractions).

may contain some structural complexity,[57,58,60,62,67,70,72,73] it was modeled as a single annular region with an average density to avoid excessive free parameters. For each filling motif, the form factor, $P_C(q)$, was investigated as a function of the polymer fill fraction, f, pore diameter, R_p, and lattice constant, a, as well as a corona thickness, $t_c = R_p − R_c$, and corona density, ρ_c. Analytical expressions for the unit cell scattering amplitude were constructed from the superposition principle of waves and approximation of each density region with a geometric shape with a known scattering law. These expressions are deferred to the Supporting Information, but we note they were validated against direct numerical Fourier transform and orientational averaging of 3-dimensional density grids for numerous representative cases (also in the SI).

The clearest qualitative impact of changes to the unit cell mesostructure can be observed from its effect on low-order diffraction intensities, which rise above the diffuse background. The effect originates in the product $P_C(q) \cdot S(q)$ in eq 1, which modulates the Bragg peak intensities (structure factor) by the magnitude of the form factor at a given q. In Figure 6b, we show the Bragg regions of the experimental scattering patterns for both sets of PEI/SBA-15 systems. These plots highlight the characteristic filling trends mentioned previously—namely, the growing asymmetry of the [10] peak and the relative intensity inversion of the [11] and [20] peaks in both systems. From eq 1, it is expected that the magnitude of the unit cell form factor should exhibit corresponding functionality. Form factors for the various morphological motifs discussed above, calculated as a function of polymer filling, are thus shown in Figure 6c. For illustration, we have simply chosen a representative set of unit cell parameters and overlaid the structure factor of the corresponding hexagonal lattice (to be multiplied by the form factor point-wise). The figure shows (i) plug and (ii) conformal annular coating models, as well as (iii) a hybrid model, whereby the first 20% vol of polymer (∼1−2 monolayers depending on roughness) is allocated to a surface coating with further addition yielding a plug in the remaining central space. It should be noted that although the proposed polymer plugs have lengths corresponding to very low q-values, a growing fraction of plug occupation along the pore is still manifested across the measured q-range: the spectrum roughly behaves as a weighted average between the two-dimensional cross-sectional spectra of regions with and without occupation by the plug.

It can be seen that in the case of a pure plug model, the asymmetry of the [10] peak would be expected to set in rapidly after relatively low filling (pending diffuse background level), while for a conformal coating or sequential coating-plug model this asymmetry would be delayed until higher fillings (as observed). Shifting focus to the higher order reflections, strong minima are evident at intermediate fill fractions in the plug and hybrid models, which will lower the [11] peak relative to the [20] peak; a strict conformal deposition will not reproduce the inversion until nearly complete filling, thus pointing to the hybrid case. Naturally, the models converge in the limit of completely full (or empty) pores.

Quantitative Fitting and Interpretation. Full-pattern fitting with eq 1 was used to estimate characteristic dimensions of the PEI/SBA-15 systems. Unit cell form factors were determined as described above. The structure factor was that of a 2-D hexagonal lattice, parametrized with a Debye−Waller factor $\langle u \rangle^2$ to account for variable displacement from ideal lattice planes (see SI). To model the myriad array of small-scale inhomogeneities contributing to $i_D(q)$, we empirically selected a
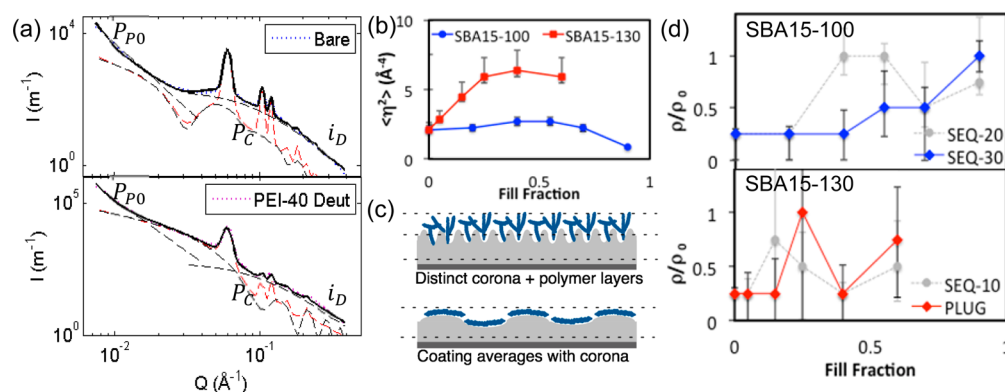
Figure 8. (a) Example fits of SANS patterns for bare SBA15−130 and 40 wt % PEI/SBA15−130. Component functions include: particle form factor $P_{P0}(q)$ at low q ($\propto q^{-4}$ here), unit cell form factor $P_C(q)$ at intermediate q, and diffuse scattering function $i_D(q)$ at high q. These are not strictly additive, per eq 1. The red line represents the product $P_C(q) \cdot S(q)$, with adjustments for polydispersity and resolution (see Supporting Information). (b) Mean-squared density fluctuations vs fill fraction, obtained from the diffuse scattering function. (c) Schematic of initial PEI coating modes whereby a distinct polymer layer may or may not be seen depending on dimensions of surface corrugations. (d) Corona density vs fill fraction for each SBA-15 material, shown for the two best-fit fill motifs. Error bars give the range of values that shift the SSR by <5% in (b) and (d).

Table 1. Structural Parameters Derived for SBA-15 Samples[a]

	PEI/SBA15−100				PEI/SBA15−130			
model	R_p (Å)	t_c (Å)	$\langle u^2 \rangle$ (Å²)	SSR	R_p (Å)	t_c (Å)	$\langle u^2 \rangle$ (Å²)	SSR
plug	31	12	100	1.15	**41**	**10**	**100**	**1.00**
sequential 10/90	33	10	160	1.09	41	8	120	1.05
sequential 20/80	33	12	200	1.04	36	16	280	1.23
sequential 30/70	**32**	**14**	**260**	**1.00**		unstable		
simultaneous 50/50	32	12	240	1.11	35	18	140	1.14
conformal		unstable				unstable		

[a]On the basis of mimimization of collective error in $I(q)$ for a PEI loading series based on different potential filling morphologies. Polymer fill models are described in the main text. Parameters are pore radius (R_p), corona thickness (t_c), Debye−Waller factor ($\langle u^2 \rangle$), and sum of squared residuals (SSR), which is normalized to the best fit. Since $I(q)$ spans multiple orders of magnitude, squared residuals were weighted by $1/|I(q)|^2$ to make all points contribute equally.

two-phase random-medium model, first described by Debye et al.[81,82] The scattering of such a system yields a squared-Lorentzian distribution defined by an effective correlation length (ξ) and the mean-squared SLD fluctuations $\eta^2 = \overline{\rho^2} - \overline{\rho}^2$:

$$i_D(q) = \frac{8\pi\xi^3 \langle \eta^2 \rangle V_S}{(1 + q^2\xi^2)^2} \qquad (2)$$

This contribution is considered to be purely additive—i.e., no coherent interference—and its intensity scales with illuminated volume, which we have defined as the solid skeletal volume, V_s (the nonmesoporous volume of the particle). Likewise, the values obtained for η^2 only correspond to fluctuations on the length scale of ξ rather than the global mean-squared fluctuations, often obtained from total spectrum integration.[60] This modeling choice is discussed further in the Supporting Information, along with treatment of corrections for instrumental resolution, polydispersity, and orientational averaging.

Because of the complexity of the total scattering law, data were fit by numerical error minimization based on a series of constrained factorial parameter sweeps. To reduce computation time, a database of unit cell form factors was first generated, incrementally spanning all realistic dimensions (pore radius, corona thickness and density etc.) for each filling motif (cf. Figure 7). Six models were considered, including the plug model, annular coating model, and four hybrids—these included three "sequential hybrids" whereby either the first 10, 20, or 30% vol were allocated to a conformal coating (setting a critical thickness) while additional polymer was allocated to a plug in the center of the annular space. A final "simultaneous hybrid" model placed equal volumes of polymer onto the pore wall and plug region, irrespective of the total fill (i.e., fill fraction was divided by two and this amount was allocated to each region). In all, ∼500 000 form factor candidates were generated.

To keep results physically transparent, we chose to fix parameters that could be determined a priori with reasonable accuracy (polymer fill fraction from physisorption, lattice constant from Bragg peak positions). We then fit parameters that are intrinsic to a given support (average pore radius, corona radius, and Debye−Waller factor) through an aggregate error minimization across each complete loading series (i.e., minimizing the sum of the sums of squared error for all patterns on a given material). For this initial step, the remaining variables (corona density, diffuse scattering parameters) were allowed to vary across fill fractions. Two sample fits derived in this manner are shown in Figure 8a, along with overlays of several component functions for visual aid. The optimum values for R_P, t_C, and $\langle u \rangle^2$ achieved in the above manner are shown in Table 1 for each filling model considered. Summed squares of residual error (SSR), normalized to the best fit, are also shown to provide a gauge for how uniquely each model fits the data.
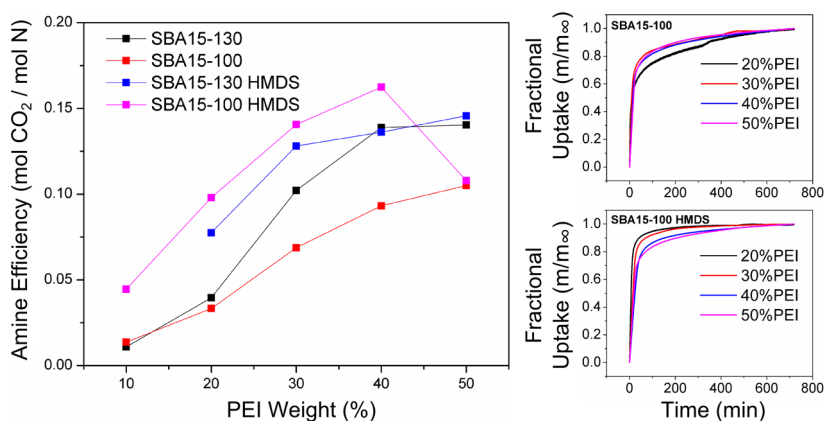
Figure 9. (a) Amine efficiency for untreated and HDMS capped PEI/SBA-15 composites. (b) CO_2 uptake over time for PEI/SBA15−100 materials before and after HDMS capping. Kinetic data on semilog axes available in Figure S5.

The fits reveal that the collective data set for the PEI/SBA15−100 series is most consistent with a sequential fill motif, in which the first 30% vol of PEI is deposited as a coating and further addition yields an aggregated plug. Conversely, it appears that the PEI/SBA-130 forms a much thinner (if any) surface coating, with the plug model yielding a marginally better fit than the thinnest layer sequential layer model (10% vol. coating). Thinner coating cases were examined for SBA15−130 but were negligibly better in fit quality—these would correspond to subnanometer features that are not resolvable. It should be noted that the fitting parameters in Table 1 represent clear optima for each filling motif (SSR vs each variable is parabolic), and that the next-best fits represent small perturbations to the optimized topology; i.e., the sequential 10−90% model is the next-best relative to the plug model for SBA15−130, while a 20−80% sequential model is second in quality to the 30−70% sequential option for SBA15−100.

Values obtained for the diffuse scattering parameters (ξ and η^2) and the corona SLD (ρ_c) as a function of PEI fill fraction shed additional light onto the polymer−silica interaction. We first note in Figure 8b that η^2 values, which represent the magnitude of spatial SLD fluctuations at the micropore scale, are effectively constant for SBA15−100 (becoming drowned out by mesopore scatter at the highest fillings), while they exhibit a clear increase with fill fraction on SBA15−130. Correlation lengths did not appreciably vary with filling (6−8 Å in SBA15−100 and 10−12 Å in SBA15−130), and the trends in η^2 provide initial evidence that the intrawall porosity is accessible to the polymer only in the case of the larger, smoother pore SBA15−130 material. This picture is corroborated by the corona SLDs, shown in Figure 8d. In the figure, we show ρ_c values (normalized to the wall density) obtained for each SBA-15 material using both the optimal fill motif as well as the "next-best" motif. In general, small increases to the corona SLD are observed upon introduction of PEI, and in most cases the SLD increase is larger and present at lower loadings for SBA15−130, as would be expected from PEI occupying the corona and raising η^2. More interestingly, by comparing to the less optimal fit motifs, a compensation effect can be seen whereby a thicker conformal coating tracks with a lower corona density, and vice versa (e.g., plug model showing higher corona SLD than the sequential model for SBA15−130). Since the pore/corona boundary is not in reality a discrete transition, this convergent behavior provides confidence in the hypothesis that an initial conformal layer is formed in both materials. We

propose that this layer is manifested as a continuous high SLD coating on SBA15−100 because the corona is relatively impermeable to PEI, save for perhaps individual side-chains that may serve as anchor points. Such an interaction would result in polymer chains that are tethered, but extend into the pore rather than lay flat. In contrast, the corona of SBA15−130 possesses larger, smooth corrugations, which can be directly occupied by PEI molecules. The initial coating will be more discontinuous in this case and have a lower average density (moving in radial increments). We display a schematic of the envisioned interactions between the two pore/corona topologies and PEI in Figure 8c. This picture is consistent with the more dramatic drop in apparent pore size in the PSD of SBA15−130 (vs SBA15−100), since wider corrugations are more likely to cause delayed condensation in the mesopore (increasing apparent diameter) than to condense N_2 independently.

CO_2 Adsorbent Design and Performance. The sequential model of pore filling inferred from the physisorption and scattering data (surface coating followed by plug formation) suggests there is in general very little freely accessible PEI in contact with the void space of the pore. At low PEI loadings, amine sites are largely unavailable due to strong interaction with the pore wall, while at higher loadings, CO_2 must diffuse through a significant volume of PEI to reach the majority of unsaturated amine sites. To date, there remain conflicting reports as to whether the pore dimensions of a mesoporous support will independently improve the amine efficiency of impregnated PEI.[20,21,23−27] Reports on the importance of PEI/surface interactions are less numerous,[22,28,29] and ambiguities along both avenues stem in part from difficulty in fixing one textural property of a support while systematically changing another. The present work implies that an optimal support (maximizing amine efficiency) may be characterized by having (i) a high specific pore volume and short pore length to minimize diffusion lengths through PEI plugs, (ii) weak PEI/surface interactions and (iii) a surface area approaching that of the geometric area of the pores (minimal corrugation) to minimize competition between CO_2 and surface sites for binding of PEI.

To evaluate the proposed design hypotheses, we post-synthetically modified the surfaces of our SBA15 materials with hexamethyldisilazane (HMDS) to convert the hydrophilic silanols to hydrophobic trimethylsilyl groups. This was expected to raise the CO_2 capacity and uptake rate by changing

the attractive interaction of the surface with PEI to a repulsive interaction, freeing up previously bound amines. It was also anticipated that higher total CO_2 capacity could highlight mass-transport limited regimes, supporting the formation of plugs. We note that while the grafted coating may close off very small intrawall pores, PSDs of the HDMS-SBA-15 materials (Figure S3) show very minor changes, with loss of volume fractions from pores only <2 nm. The present data indicate PEI does not appreciably enter such spaces. Thus, the accessibility of amine sites is more likely to reflect PEI-surface interactions.

Figure 9 shows amine efficiencies collected at 400 ppm of CO_2 for a PEI-loading series (commercial h-PEI) of SBA15−100 and SBA15−130 with and without HDMS capping, as well as uptake vs time (normalized to equilibrium capacity) for the SBA15−100 materials. In both cases the HDMS treatment clearly increases the total CO_2 capacity, with post-treatment capacities being very similar for both materials at low loadings. The SBA15−130 has a less dramatic enhancement, as this substrate is inherently less prone to inhibition due to lower surface-area. The performance of SBA15−130 also appears to converge with that of its HDMS-capped counterpart at higher PEI loading, likely because the bound amines represent a smaller fraction of the total available sites. Despite the overall enhancements, the two HDMS-capped materials show a divergence in capacity in the high-loading limit. This limit represents nearly filled pores for the SBA15−100 while there is still substantial free space in the SBA15−130. Thus, we hypothesize that the PEI plug component reaches a critical length in SBA15−100, at which point true adsorption equilibration becomes unachievable on the experimental time scale. We suggest that this regime could set in rather abruptly since there may exist a compound effect between increased diffusion length and decreased diffusivity, caused by polymer cross-linking in the course of saturation.[39,40]

The trends in CO_2 capacity are consistent with rates of pseudoequilibration, demonstrated for SBA15−100 in Figure 9b. We first note that the low PEI-loading samples show a significant increase in equilibration rate upon functionalization with HDMS. The equilibration rates increase for each sample up to and including 40 wt %, while the fully pore-blocked 50 wt % sample shows essentially identical performance before and after capping. We suggest that while the HDMS-capped sorbent should have more free-amines available for binding, a greater degree of saturation with CO_2 may lower the diffusivity of gas through PEI and undermine the increased site availability. It is also conceivable that the microporous corona region of the SBA15−100 could actually aid in gas transport and that this benefit is lost upon closure of the micropores with HDMS. This notion would be supported by the fact that the uncapped SBA15−130, which possesses less microporosity than SBA15−100, already shows a drop in saturation rate at 50 wt %, which represents only about 60% pore filling for the material (kinetic data for SBA15−130 in Figure S4). While the diffusional impediments at higher amine-loadings are modest in our model silica, these materials also possesses relatively short, linear transport paths. Commercial silicas that are practical for scale-up generally possess longer, tortuous pores, and in applications such as membrane separations, diffusion paths can be as much as 1−2 orders of magnitude greater.[40,83]

CONCLUSIONS

Small angle neutron scattering and physisorption analyses have suggested that in PEI/silica composite adsorbents, PEI initially forms a conformal coating on the pore walls, then begins to form plug-like aggregates at higher loading. The preferred filling motif likely relates to a relatively high surface tension of PEI and preference for the molecules to remain in a bulk-polymer-like state when they cannot directly contact the strongly interacting pore wall. Scattering length density profiles fit to the data indicate that the nature of the coating may be highly compact or more diffuse depending on the roughness and intrawall porosity of a given silica material. The filling model ultimately points to a trade-off between high chemical accessibility of the amine binding sites, which are inaccessible when they bind to silica, and high accessibility for mass transport, which can be hampered by diffusion through PEI plugs. We have illustrated this design principle by demonstrating higher CO_2 capacity and uptake rate for PEI supported in a hydrophobically coated silica, yielding repulsive wall interactions. While such materials may introduce new complications (e.g., stability loss from PEI leaching), appropriate responses (e.g., mixed-functionality coatings with anchoring sites) can also be envisioned. Such architectures may permit design of sorbent systems with faster CO_2 concentration capability and improved energy efficiency.

ASSOCIATED CONTENT

Supporting Information

The Supporting Information is available free of charge on the ACS Publications website at DOI: 10.1021/jacs.5b06823.

> Supplementary adsorbent characterization, including summary of textural properties for all PEI/SBA-15 samples, physisorption isotherms of d-PEI/SBA-15 adsorbents, comparison of CO_2 adsorption on SBA-15 composites with h-PEI vs d-PEI, pore size distributions of HDMS-capped PEI/SBA-15 adsorbents, and CO_2 adsorption vs time on PEI/SBA15−130 and PEI/SBA15−130-HDMS. SANS modeling details, and synthesis and characterization of d-PEI are also provided. (PDF)

AUTHOR INFORMATION

Corresponding Author
*cjones@chbe.gatech.edu

Notes
The authors declare no competing financial interest.

ACKNOWLEDGMENTS

REFERENCES

(1) Long, W.; Brunelli, N. A.; Didas, S. A.; Ping, E. W.; Jones, C. W. *ACS Catal.* **2013**, *3*, 1700.
(2) Brunelli, N. A.; Didas, S. A.; Venkatasubbaiah, K.; Jones, C. W. *J. Am. Chem. Soc.* **2012**, *134*, 13950.

(3) Das, D. D.; Sayari, A. J. Catal. 2007, 246 (1), 60.

(4) Choi, S.; Drese, J. H.; Jones, C. W. ChemSusChem 2009, 2, 796.

(5) Drese, J. H.; Talley, A. D.; Jones, C. W. ChemSusChem 2011, 4, 379.

(6) Sayari, A.; Hamoudi, S.; Yang, Y. Chem. Mater. 2005, 17 (1), 212.

(7) Serna-Guerrero, R.; Sayari, A. Environ. Sci. Technol. 2007, 41 (13), 4761.

(8) Nomura, A.; Jones, C. W. ACS Appl. Mater. Interfaces 2013, 5 (12), 5569.

(9) Belmabkhout, Y.; Serna-Guerrero, R.; Sayari, A. Ind. Eng. Chem. Res. 2010, 49, 359.

(10) Tailor, R.; Abboud, M.; Sayari, A. Environ. Sci. Technol. 2014, 48 (3), 2025.

(11) Xu, X.; Song, C.; Andresen, J. M.; Miller, B. G.; Scaroni, A. W. Energy Fuels 2002, 16 (18), 1463.

(12) Bollini, P.; Didas, S. A.; Jones, C. W. J. Mater. Chem. 2011, 21, 15100.

(13) Dutcher, B.; Fan, M.; Russell, A. G. ACS Appl. Mater. Interfaces 2015, 7 (4), 2137.

(14) Chen, C.; Kim, J.; Ahn, W.-S. Korean J. Chem. Eng. 2014, 31 (11), 1919.

(15) Hedin, N.; Chen, L.; Laaksonen, A. Nanoscale 2010, 2 (10), 1819.

(16) McNutt, M. K.; Abdalati, W.; Caldeira, K.; Doney, S. C.; Falkowski, P. G. Climate Intervention: Carbon Dioxide Removal and Reliable Sequestration; National Academies Press: Washington, D.C., 2015; p 141.

(17) Eisenberger, P. M.; Cohen, R. W.; Chichilnisky, G.; Eisenberger, N. M.; Chance, R. R.; Jones, C. W. Energy Environ. 2009, 20, 973.

(18) Zhao, D.; Feng, J.; Huo, Q.; Melosh, N.; Fredrickson, G.; Chmelka, B.; Stucky, G. Science (Washington, DC, U. S.) 1998, 279, 548.

(19) Zhao, D.; Huo, Q.; Feng, J.; Chmelka, B. F.; Stucky, G. D. J. J. Am. Chem. Soc. 1998, 120 (5), 6024.

(20) Zhang, H.; Goeppert, A.; Czaun, M.; Prakash, G. K. S.; Olah, G. A. RSC Adv. 2014, 4 (37), 19403.

(21) Wang, D.; Wang, X.; Ma, X.; Fillerup, E.; Song, C. Catal. Today 2014, 233, 100.

(22) Kuwahara, Y.; Kang, D. Y.; Copeland, J. R.; Brunelli, N. A.; Didas, S. A.; Bollini, P.; Sievers, C.; Kamegawa, T.; Yamashita, H.; Jones, C. W. J. J. Am. Chem. Soc. 2012, 134, 10757.

(23) Vilarrasa-Garcia, E.; Moya, E. M. O.; Cecilia, J. a.; Cavalcante, C. L.; Jiménez-Jiménez, J.; Azevedo, D. C. S.; Rodríguez-Castellón, E. Microporous Mesoporous Mater. 2014, 209, 172.

(24) Yan, X.; Zhang, L.; Zhang, Y.; Yang, G.; Yan, Z. Ind. Eng. Chem. Res. 2011, 50, 3220.

(25) Wang, L.; Yao, M.; Hu, X.; Hu, G.; Lu, J.; Luo, M.; Fan, M. Appl. Surf. Sci. 2015, 324, 286.

(26) Heydari-Gorji, A.; Yang, Y.; Sayari, A. Energy Fuels 2011, 25, 4206.

(27) Yan, X.; Komarneni, S.; Yan, Z. J. J. Colloid Interface Sci. 2013, 390 (1), 217.

(28) Heydari-Gorji, A.; Belmabkhout, Y.; Sayari, A. Langmuir 2011, 27, 12411.

(29) Yue, M. B.; Chun, Y.; Cao, Y.; Dong, X.; Zhu, J. H. Adv. Funct. Mater. 2006, 16 (13), 1717.

(30) Cogswell, C. F.; Jiang, H.; Ramberger, J.; Accetta, D.; Willey, R. J.; Choi, S. Langmuir 2015, 31, 4534.

(31) Sakwa-Novak, M. A.; Jones, C. W. ACS Appl. Mater. Interfaces 2014, 6, 9245.

(32) Donaldson, T. L.; Nguyen, Y. N. Ind. Eng. Chem. Fundam. 1980, 19, 260.

(33) Pinto, L.; Mafra, L.; Guil, J. M.; Pires, J.; Rocha, J. Chem. Mater. 2011, 23, 1387.

(34) Danon, A.; Stair, P. C.; Weitz, E. J. J. Phys. Chem. C 2011, 115, 11540.

(35) Bacsik, Z.; Ahlsten, N.; Ziadi, A.; Zhao, G.; Garcia-bennett, A. E.; Martin-Matute, B.; Hedin, N. Langmuir 2011, 27, 11118.

(36) Espinal, L.; Green, M. L.; Fischer, D. A.; Delongchamp, D. M.; Jaye, C.; Horn, J. C.; Sakwa-Novak, M. A.; Chaikittisilp, W.; Brunelli, N. A.; Jones, C. W. J. Phys. Chem. Lett. 2015, 6, 148.

(37) Bollini, P.; Brunelli, N. A.; Didas, S. A.; Jones, C. W. Ind. Eng. Chem. Res. 2012, 51, 15153.

(38) Wilfong, W. C.; Chuang, S. S. C. Ind. Eng. Chem. Res. 2014, 53, 4224.

(39) Wilfong, W. C.; Srikanth, C. S.; Chuang, S. S. C. ACS Appl. Mater. Interfaces 2014, 6, 13617.

(40) Kim, H.; Chaikittisilp, W.; Jang, K.-S.; Didas, S. A.; Johnson, J. R.; Koros, W. J.; Nair, S.; Jones, C. W. Ind. Eng. Chem. Res. 2015, 54, 4407.

(41) Blin, J. L.; Impéror-Clerc, M. Chem. Soc. Rev. 2013, 42 (42), 4071.

(42) Solovyov, L. A. Chem. Soc. Rev. 2013, 42, 3708.

(43) Liu, Z.; Terasaki, O.; Ohsuna, T.; Hiraga, K.; Shin, H. J.; Ryoo, R. ChemPhysChem 2001, 2 (4), 229.

(44) Ryoo, R.; Ko, C. H.; Kruk, M.; Antochshuk, V.; Jaroniec, M. J. J. Phys. Chem. B 2000, 104, 11465.

(45) Imperor-Clerc, M.; Davidson, P.; Davidson, A. J. J. Am. Chem. Soc. 2000, 122 (16), 11925.

(46) Galarneau, A.; Cambon, H.; Di Renzo, F.; Fajula, F. Langmuir 2001, 17 (26), 8328.

(47) Kruk, M.; Jaroniec, M.; Ko, C. H.; Ryoo, R. Chem. Mater. 2000, 12 (7), 1961.

(48) Lee, H. I.; Kim, J. H.; Stucky, G. D.; Shi, Y.; Pak, C.; Kim, J. M. J. Mater. Chem. 2010, 20, 8483.

(49) Thommes, M.; Cychosz, K. A. Adsorption 2014, 20 (2−3), 233.

(50) Landers, J.; Gor, G. Y.; Neimark, A. V. Colloids Surf., A 2013, 437, 3.

(51) Zhao, J. K.; Gao, C. Y.; Liu, D. J. J. Appl. Crystallogr. 2010, 43, 1068.

(52) Thommes, M. Chem. Ing. Tech. 2010, 82 (7), 1059.

(53) Brunauer, S.; Emmett, P. H.; Teller, E. J. J. Am. Chem. Soc. 1938, 60 (1), 309.

(54) Monson, P. A. Microporous Mesoporous Materials 2012, 16, 47.

(55) Drese, J. H.; Choi, S.; Lively, R. P.; Koros, W. J.; Fauth, D. J.; Gray, M. L.; Jones, C. W. Adv. Funct. Mater. 2009, 19, 3821.

(56) Sanz, R.; Calleja, G.; Arencibia, A.; Sanz-Pérez, E. S. Microporous Mesoporous Mater. 2012, 158, 309.

(57) Pollock, R. A.; Walsh, B. R.; Fry, J.; Ghampson, I. T.; Melnichenko, Y. B.; Kaiser, H.; Pynn, R.; Desisto, W. J.; Wheeler, M. C.; Frederick, B. G. Chem. Mater. 2011, 23, 3828.

(58) Jähnert, S.; Müter, D.; Prass, J.; Zickler, G. A.; Paris, O.; Findenegg, G. H. J. J. Phys. Chem. C 2009, 113, 15201.

(59) Müter, D.; Jähnert, S.; Dunlop, J. W. C.; Findenegg, G. H.; Paris, O.; Mü, D.; Jähnert, S.; Dunlop, J. W. C.; Findenegg, G. H.; Paris, O. J. J. Phys. Chem. C 2009, 113, 15211.

(60) Findenegg, G. H.; Jähnert, S.; Müter, D.; Prass, J.; Paris, O. Phys. Chem. Chem. Phys. 2010, 12, 7211.

(61) Vogt, B. D.; Pai, R. A.; Lee, H.; Hedden, R. C.; Soles, C. L.; Wu, W.; Lin, E. K.; Bauer, B. J.; Watkins, J. J. Chem. Mater. 2005, 17, 1398.

(62) Edler, K. J.; Reynolds, P. A.; White, W.; Cookson, D.; White, J. W.; Cookson, D. J. J. Chem. Soc., Faraday Trans. 1997, 93, 199.

(63) Hammond, W.; Prouzet, E.; Mahanti, S. D.; Pinnavaia, T. J. Microporous Mesoporous Mater. 1999, 27, 19.

(64) Jaroniec, M.; Solovyov, L. A. Langmuir 2006, 22 (8), 6757.

(65) Muroyama, N.; Ohsuna, T.; Ryoo, R.; Kubota, Y.; Terasaki, O. J. J. Phys. Chem. B 2006, 110, 10630.

(66) Pikus, S.; Solovyov, L. A.; Kozak, M.; Jaroniec, M. Appl. Surf. Sci. 2007, 253, 5682.

(67) Sauer, J.; Marlow, F.; Schüth, F. Phys. Chem. Chem. Phys. 2001, 3, 5579.

(68) Solovyov, L. A.; Kirik, S. D.; Shmakov, A. N.; Romannikov, V. N. Microporous Mesoporous Mater. 2001, 44−45, 17.

(69) Albouy, P. A.; Aryal, A.; Ayral, A. Chem. Mater. 2002, 14, 3391.

(70) Hofmann, T.; Wallacher, D.; Huber, P.; Birringer, R.; Knorr, K.; Schreiber, A.; Findenegg, G. H. Phys. Rev. B: Condens. Matter Mater. Phys. 2005, 72, 1.

(71) Schreiber, A.; Ketelsen, I.; Findenegg, G. H.; Hoinkis, E.; Llewellyn, P. L.; Rodriquez-Reinoso, F.; Rouqerol, J.; Schreiber, A.; Ketelsen, I.; Findenegg, G. H.; Hoinlds, E.; Hoinkis, E. *Stud. Surf. Sci. Catal.* **2007**, *160*, 17.

(72) Zickler, G. A.; Jähnert, S.; Wagermaier, W.; Funari, S. S.; Findenegg, G. H.; Paris, O. *Phys. Rev. B: Condens. Matter Mater. Phys.* **2006**, *73*, 1.

(73) Edler, K. J.; Reynolds, P. A.; White, J. W. J. *J. Phys. Chem. B* **1998**, *102* (97), 3676.

(74) Mascotto, S.; Wallacher, D.; Brandt, A.; Hauss, T.; Thommes, M.; Zickler, G. A.; Funari, S. S.; Timmann, A.; Smarsly, B. M. *Langmuir* **2009**, *25* (13), 12670.

(75) Smarsly, B.; Göltner, C.; Antonietti, M.; Ruland, W.; Hoinkis, E.; Go, C.; Antonietti, M.; Ruland, W.; Hoinkis, E. J. *J. Phys. Chem. B* **2001**, *105*, 831.

(76) Erko, M.; Wallacher, D.; Brandt, A.; Paris, O. J. *J. Appl. Crystallogr.* **2010**, *43*, 1.

(77) Müter, D.; Shin, T.; Demé, B.; Fratzl, P.; Paris, O.; Findenegg, G. H. *J. Phys. Chem. Lett.* **2010**, *1*, 1442.

(78) Shin, T. G.; Müter, D.; Meissner, J.; Paris, O.; Findenegg, G. H. *Langmuir* **2011**, *27*, 5252.

(79) Sears, V. F. *Neutron News* **1992**, *3* (3), 26.

(80) Glatter, O. J. *J. Appl. Crystallogr.* **1979**, *12*, 166.

(81) Debye, P.; Bueche, A. M. *J. Appl. Phys.* **1949**, *20* (1949), 518.

(82) Debye, P.; Anderson, H. R.; Brumberger, H. *J. Appl. Phys.* **1957**, *28* (1957), 679.

(83) Fan, Y.; Kalyanaraman, J.; Labreche, Y.; Rezaei, F.; Lively, R. P.; Real, M. J.; Koros, W. J.; Jones, C. W.; Kawajiri, Y.; Realff, M. J.; Koros, W. J.; Jones, C. W.; Kawajiri, Y. *Ind. Eng. Chem. Res.* **2015**, *54*, 1783.